Supporting Information

Self-Assembly of Noble Metal Nanoparticles into Sub-100 nm Colloidosomes with Collective Optical and Catalytic Properties

Lei Zhang, Qikui Fan, Xiao Sha, Ping Zhong, Jie Zhang, Yadong Yin, and Chuanbo Gao*

L. Zhang, Q. Fan, X. Sha, P. Zhong, Prof. C. Gao

Centre for Materials Chemistry, Frontier Institute of Science and Technology, Xi'an Jiaotong University, Xi'an, Shaanxi 710054, China
E-mail: gaochuanbo@mail.xjtu.edu.cn
J. Zhang
School of Materials Science and Engineering, Xi'an Jiaotong University, Xi'an, Shaanxi 710049, China
Prof. Y. Yin
Department of Chemistry, University of California, Riverside, California 92521, USA

1. Additional Experimental Details

1.1 Synthesis of Au-Pt colloidosomes. In a typical synthesis of Au-Pt colloidosomes, 9.6 mL of the stock solution of the Au seeds, 960 µL of diethylamine (DEA), 420 µL of $H_2PtCl_6 \cdot 6H_2O$ (0.0625 M) and 9.6 mL of ascorbic acid (AA, 10 mM) were added into 96 mL of H_2O in order under vigorous stirring at 50 ºC. The reaction was allowed to proceed for 24 h. The resulting Au-Pd colloidosomes were then collected by centrifugation and washed with H_2O for 5 times.

1.2 Synthesis Pd-Pt colloidosomes. In a typical synthesis of Pd colloidosomes, 9.6 mL of the stock solution of the Pd seeds, 960 µL of DEA, 480 µL of H_2PdCl_6 (0.0625 M) and 9.6 mL of AA (10 mM) were added into 96 mL of H_2O in order under vigorous stirring at 50 ºC. The reaction was allowed to proceed for 24 h. The resulting Pd-Pt colloidosomes were then collected by centrifugation and washed with H_2O for 5 times.

1.3 Synthesis of Au nanoparticles for SERS. In a typical synthesis of Au nanoparticles (~ 30 nm), 1.6 mL of the stock solution of the Au seeds, 80 µL of $HAuCl_4$ (0.25 M), and 250 µL of ascorbic acid (AA, 0.1M) were added into 16 mL of H_2O in order under vigorous stirring at room temperature (25 ºC). The reaction was allowed to proceed for 20 min. The resulting Au nanoparticles were then collected by centrifugation and washed with H_2O for 5 times. The size of the Au nanoparticles can be tuned by adjusting the volume of the seed solution.

1.4 Preparation of the substrates for SERS analysis. The substrates for SERS analysis were prepared by dropping the same quantity of Au colloidosomes and Au nanospheres on clean silicon wafers (8 mm × 8 mm). The same quantity of the Au colloidosomes and Au nanospheres was ensured by adjusting the quantity of the Au seeds in the synthesis, according to the following calculations.
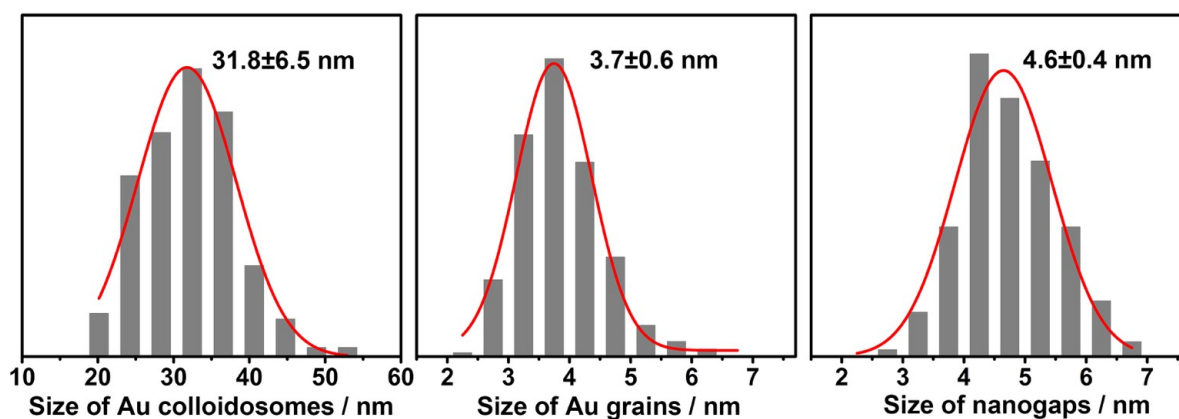
Figure S1. Histograms of the size of the Au colloidosomes, Au grains and nanogaps, respectively.

Given:

$d_{colloidosome}$—Diameter of Au colloidosomes measured from TEM images;

d_{grain}—Size of Au nanoparticle grains measured from TEM images of Au colloidosomes;

$d_{nanogap}$—Size of nanogaps measured from TEM images of Au colloidosomes;

N_0—Number of Au seeds (nanoparticles grains) included in an individual Au colloidosome;

N—Number of Au colloidosomes;

N_{seeds}—Number of Au seeds injected into the reaction system (*i.e.* Number of Au nanospheres); Assume that no self-nucleation events occurred during the seeded growth.

$N_0 = 4\pi(d_{colloidosome} / 2)^2 / \{\pi[(d_{grain} + d_{nanogap}) / 2]^2\}$

$= 4 \times (31.8 \text{ nm}/2)^2 / [(3.7 \text{ nm} + 4.6 \text{ nm}) / 2]^2$

≈ 59

Therefore, from a single batch of the synthesis, the number of the nanoparticles obtained follows the relationship of $N_{seeds}/N = 59$. By taking this relationship into consideration, the concentrations of the Au nanospheres and the colloidosomes could be adjusted to the same for SERS analysis.

1.5 Finite-difference time-domain (FDTD) simulation. The three-dimensional FDTD simulation was used to calculate the electromagnetic field distributions of the Au colloidosomes. A single Au colloidosome was modeled, which was irradiated by a plane wave at a wavelength of 633 nm. The surrounding medium of the model structure was set to be water. All simulations were performed with Lumerical FDTD Solutions (We thank Professor Liqing Huang at School of Science, Xi'an Jiaotong University for access of the software).

1.6 Disassembly of Au-Pd alloy colloidosomes. In a typical disassembly process, 200 μL of DEA was added to 1 mL of the Au-Pd alloy colloidosomes. The colloid was kept at room temperature overnight. The resulting nanoparticles were then collected by centrifugation and washed repetitively with water.

1.7 Oxygen reduction reaction (ORR): The ECSA was calculated by the area of the hydrogen desorption peak after double-layer correction in the cyclic voltammogram (CV) measurement performed in N_2-saturated 0.5 M H_2SO_4, with a reference value of 210 μC·cm^{-2}.[1] The Pd-Pt alloy colloidosomes were supported on carbon black (Cabot, Vulcan XC-72) with a metal

loading of ~ 20 %. Commercial Pt/C (JM, 20 % Pt/XC72R, HiSPEC 3000, < 3.5 nm) was used as a control catalyst. The homogeneous catalyst ink was prepared by sonicating the catalysts in a mixture solution (isopropanol : deionized water : 5 wt% Nafion = 1 : 4 : 0.02), which was followed by sonication for 60 min (Pt concentration, 0.2 $g \cdot L^{-1}$ determined by ICP-MS). The inks were prepared the night before and stirred overnight before casting the films. Then, 20 µL (Pt, 4 µg) of the ink was dropped onto the RDE and dried rotationally at a rate of 700 rpm at room temperature in air for ~ 30 min. Before electrocatalytic experiments, the working electrode was conditioned by continuous cyclic voltammetric cycles in 0.1 M $HClO_4$ (500 $mV \cdot s^{-1}$) until a stable CV curve was obtained. ORR was carried out in 0.1 M $HClO_4$ at 30 °C. The background current was measured by running the linear sweep voltammetry profile (0.05 V→1.03 V at 10 $mV \cdot s^{-1}$ and 1600 rpm) in N_2-saturated 0.1 M $HClO_4$ before the ORR measurements. This background current was subtracted from the experimental ORR currents. The electrolyte (0.1 M $HClO_4$) was saturated for at least 30 min with O_2. Ohmic resistance was determined to be ~ 20 Ω by electrochemical impedance spectroscopy (EIS) for *iR* correction. ORR polarization curves were recorded at a sweep rate of 10 $mV \cdot s^{-1}$ (0.05→1.03 V) and a rotation rate of 1600 rpm. To examine the durability, the catalysts were swept for 2000 cycles in a range of 0.6–1.05 V at a scan rate of 50 $mV \cdot s^{-1}$ and a rotation rate of 1600 rpm in O_2-saturated 0.1 M $HClO_4$; ORR polarization and CV measurements were then conducted after sweeping.

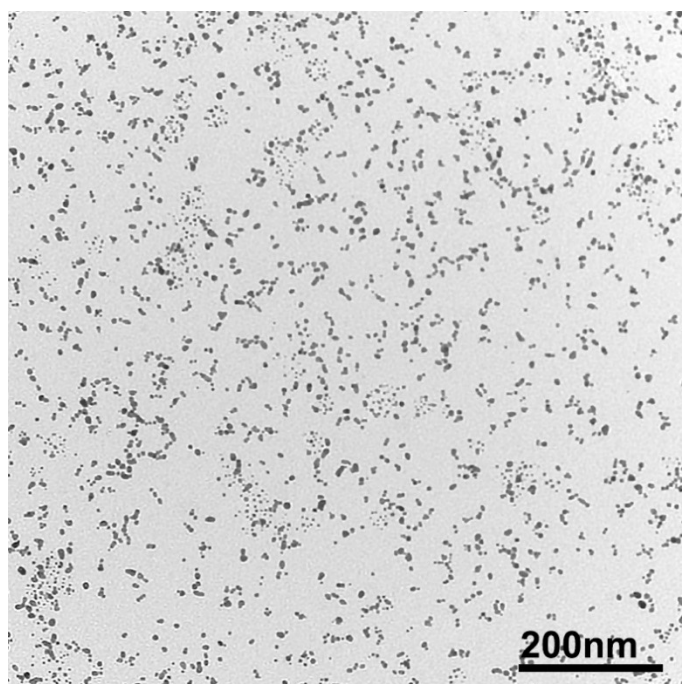**2. Supporting Information on the Synthesis of the colloidosomes.**

Figure S2. TEM image of the product obtained from a typical synthesis of Au-Pd colloidosomes without adding DEA. It can be inferred that DEA plays a critical role in microphase separation of PVP and thus formation of the self-assembled colloidosomes.
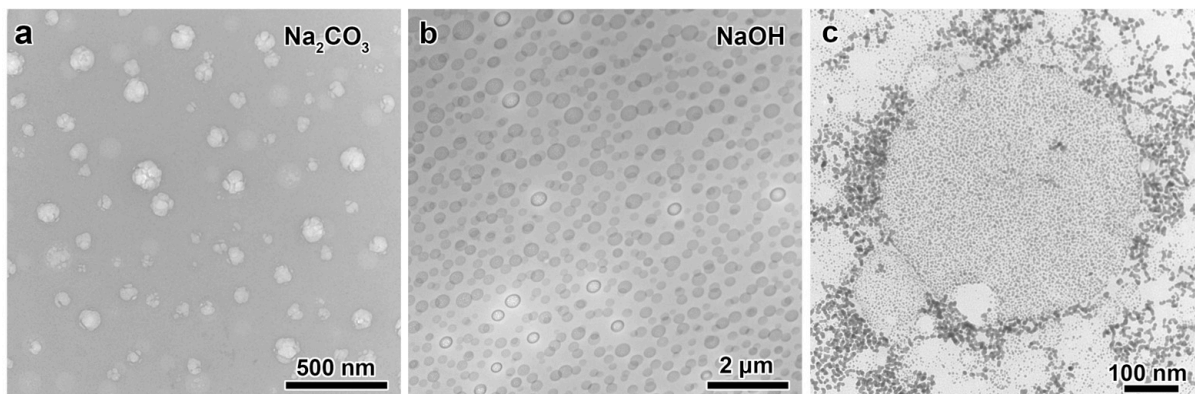
Figure S3. (a–b) TEM images of the PVP emulsion obtained by using Na_2CO_3 (a) or NaOH (b) in place of DEA. (c) TEM image of Au colloidosomes synthesized by templating against the PVP emulsion induced by addition of NaOH. Large spherical assemblies can be found, consistent with the large size of the emulsion templates. The large assemblies are unstable, which tend to break up during preparation.

Discussion on the formation of the PVP emulsion as the templates of the colloidosomes (Figure S2–S3): In this work, the PVP emulsion was formed after addition of DEA into an aqueous solution of PVP, which was evidenced by dynamic light scattering and TEM imaging after stained with Lugol's iodine. The formation of the PVP emulsion was believed to be induced by the alkalinity of DEA. To prove it, we first investigated the synthesis without DEA (Figure S2). The results indicate that Au colloidosomes failed to form in the absence of DEA. We further replaced DEA by many other types of bases, such as Na_2CO_3 and NaOH (Figure S3). The results suggest that PVP emulsion can be induced by both bases, thus confirming the critical role of the alkalinity in the formation of the PVP emulsion. However, the PVP emulsion induced by Na_2CO_3 and NaOH are much larger in size than that induced by DEA. We therefore chose DEA as a base in our experiments, which affords uniform PVP emulsion (~ 30 nm) for templated synthesis of colloidosomes. We believe that the formation of the PVP emulsion was induced by the weakened hydrogen bonding between PVP and water under an alkaline condition, which leads to a decrease in the solubility of PVP in water and thus a microphase separation.
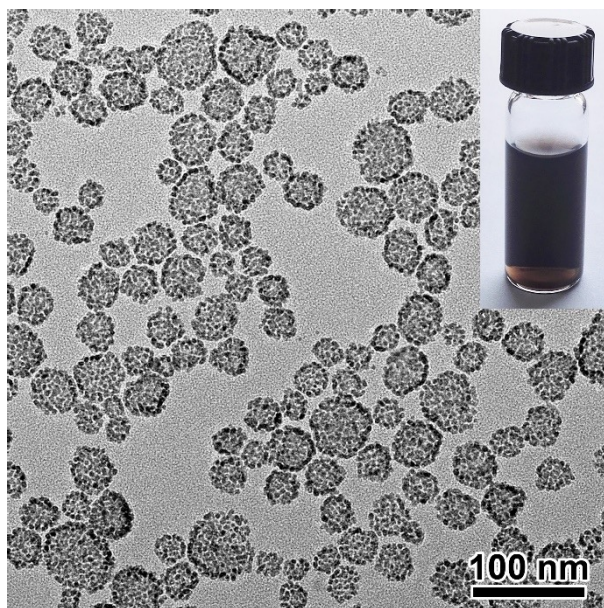
Figure S4. TEM image of the Au-Pd alloy colloidosomes. Inset: A digital photograph of a colloid of the Au-Pd alloy colloidosomes.
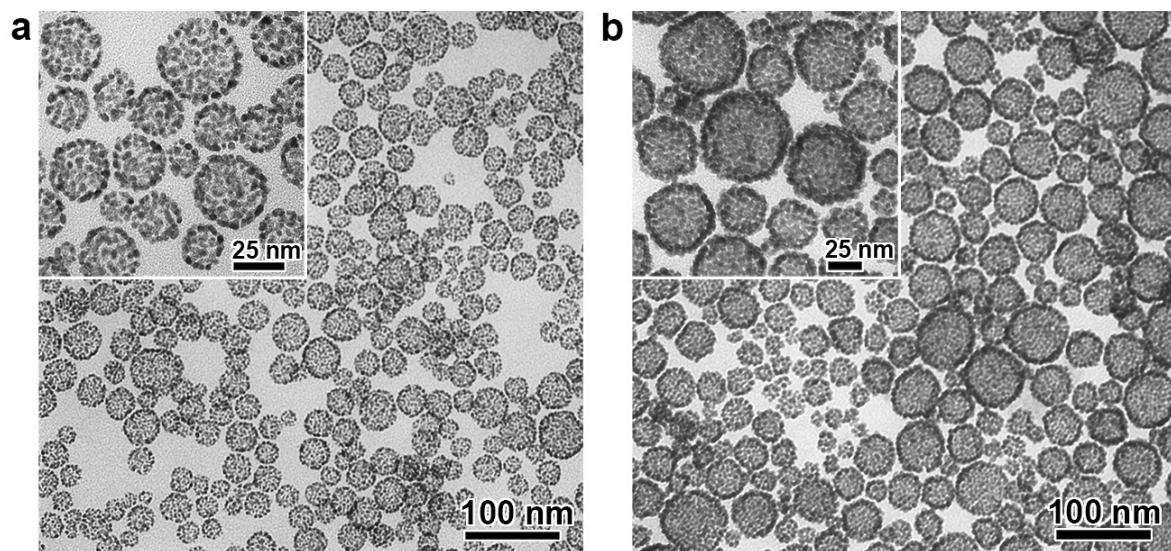
Figure S5. Tuning the morphology of the Au-Pd alloy colloidosomes by varying the concentration of the Au seeds. The concentration of the Au seeds was tuned by adjusting the concentration of $HAuCl_4$ (a, 0.25 M; b, 0.1 M) in a typical procedure (Experimental Section). With increasing concentration of the Au seeds, smaller Au-Pd alloy colloidosomes can be stabilized. It therefore confirms the critical role of the metal seeds in tuning the size of the colloidosomes.
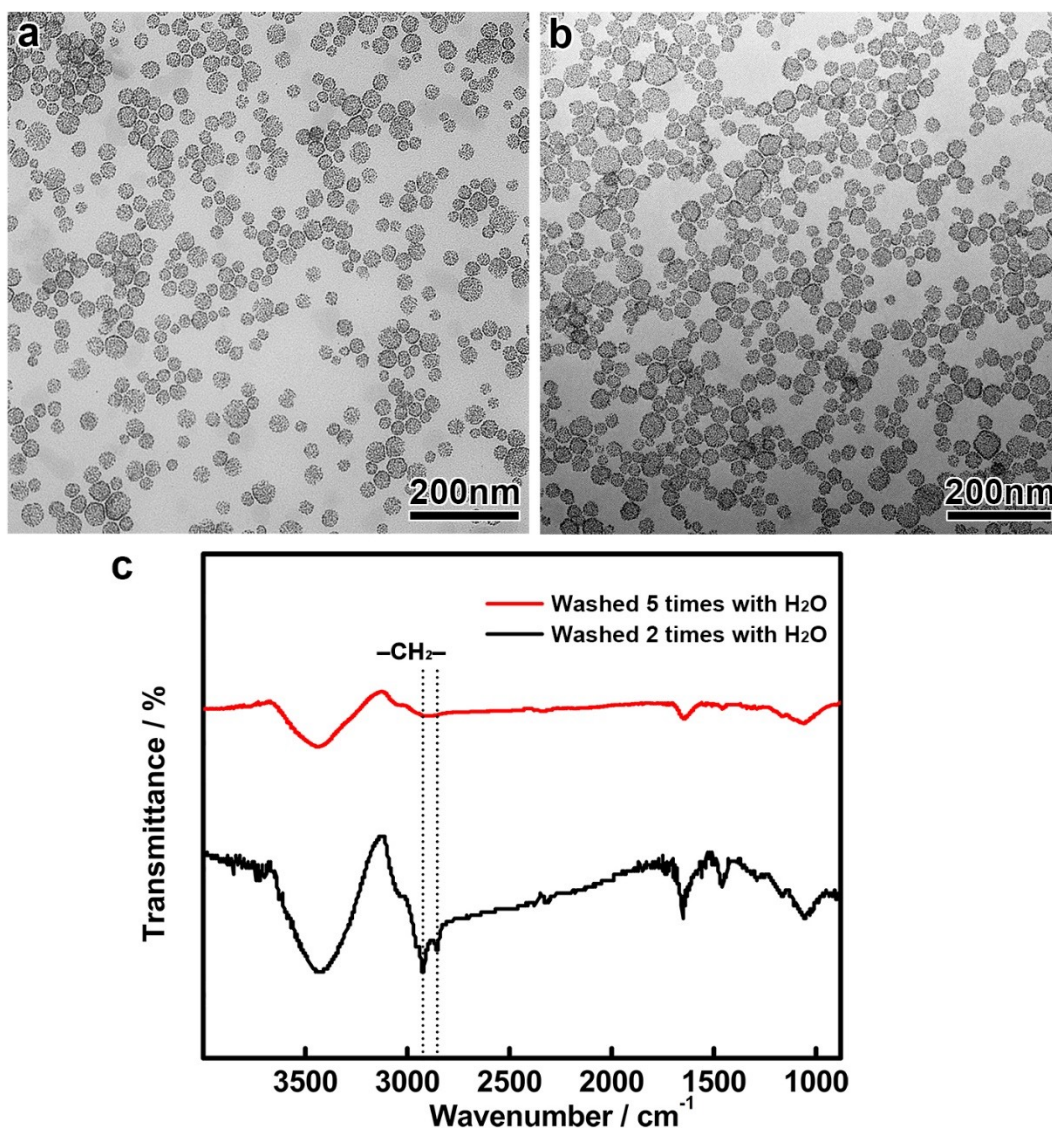
Figure S6. Partial removal of PVP from the colloidosomes by cleaning with water, taking Au-Pd alloy colloidosomes as an example. (a–b) TEM images of the Au-Pd colloidosomes after washing with H_2O for 2 and 5 times, respectively. It can be inferred that the morphological integrity of the colloidosomes has been retained during the cleaning process. (c) Fourier transform infrared spectra (FTIR) of the Au-Pd colloidosomes after washing with H_2O, respectively. Part of PVP remained in the colloidosomes after cleaning with H_2O for 2 times, and a majority of the PVP was removed from the Au-Pd colloidosomes after washing with H_2O for 5 times, which can be indicated by the vibrational peaks from the methylene groups
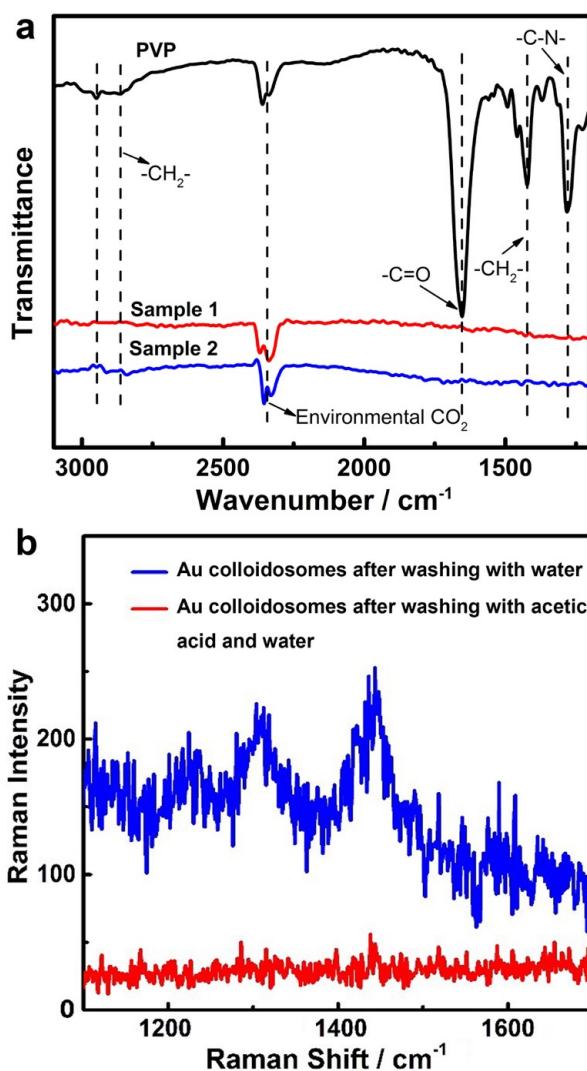
Figure S7. Complete removal of PVP from the colloidosomes by further treatment with acetic acid after repetitive washing with water. (a) FTIR spectra of PVP and the samples after treatment with acetic acid are demonstrated (Sample 1). The FTIR confirms that no residual PVP was retained in the colloidosomes. It is therefore concluded that the cleaning process by acetic acid represents a simple, convenient, and mild way to remove PVP efficiently from the samples, which is prerequisite for their applications in SERS and electrochemical catalysis. In addition, the FTIR spectrum of the disassembled colloidosomes after the treatment with acetic acid was also presented (Sample 2). The FTIR spectroscopy confirmed that PVP was completely removed from this sample after the treatment. (b) SERS spectra of Au colloidosomes after cleaning with water, and Au colloidosomes after cleaning with acetic acid and water. After cleaning with water, Raman signals from PVP can be still detectable. In clear contrast, no signals remain after washing acetic acid. It confirms again that cleaning with acetic acid represents an efficient way to remove PVP from the samples.
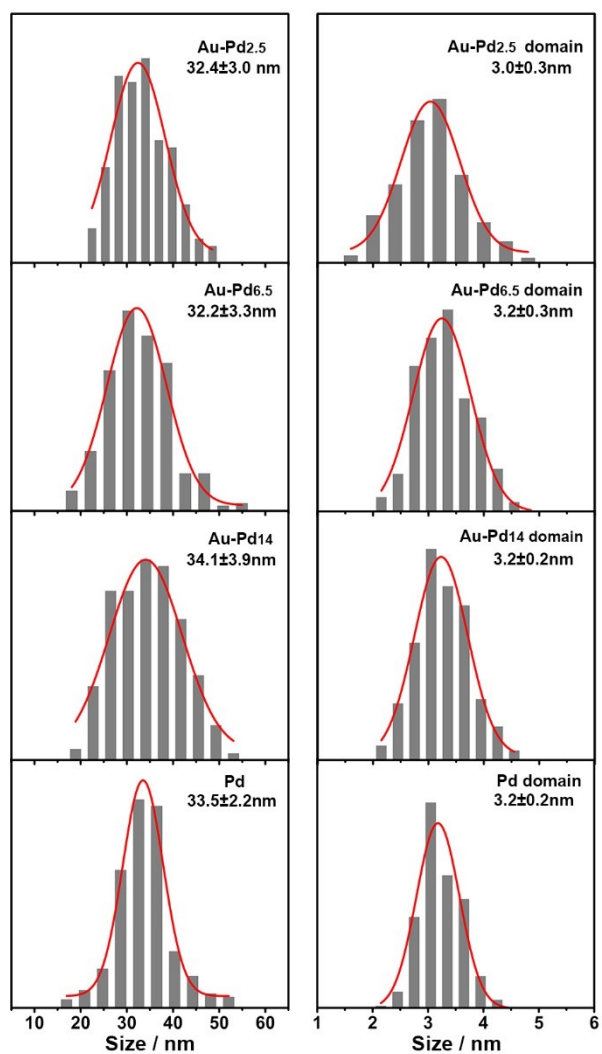
Figure S8. Size distributions of the nanoparticle grains in the colloidosomes, measured from their HRTEM images.

Table S1. Elemental analysis of the colloidosomes by ICP-MS.

Entry	Atomic ratio determined by ICP-MS	Atomic ratio in the precursor during the synthesis
Au-Pd colloidosomes	Pd/Au = 0.53	Pd/Au = 6.25
Au-Pd colloidosomes	Pd/Au = 2.52	Pd/Au = 12.5
Au-Pd colloidosomes	Pd/Au = 6.5	Pd/Au = 25
Au-Pd colloidosomes	Pd/Au = 14	Pd/Au = 50
Pd-Pt colloidosomes	Pt/Pd = 2.17	Pt/Pd = 6.25
Au-Pt colloidosomes	Pt/Au = 1.83	Pt/Au = 10.94

3. Supporting Information on the SERS Experiments.
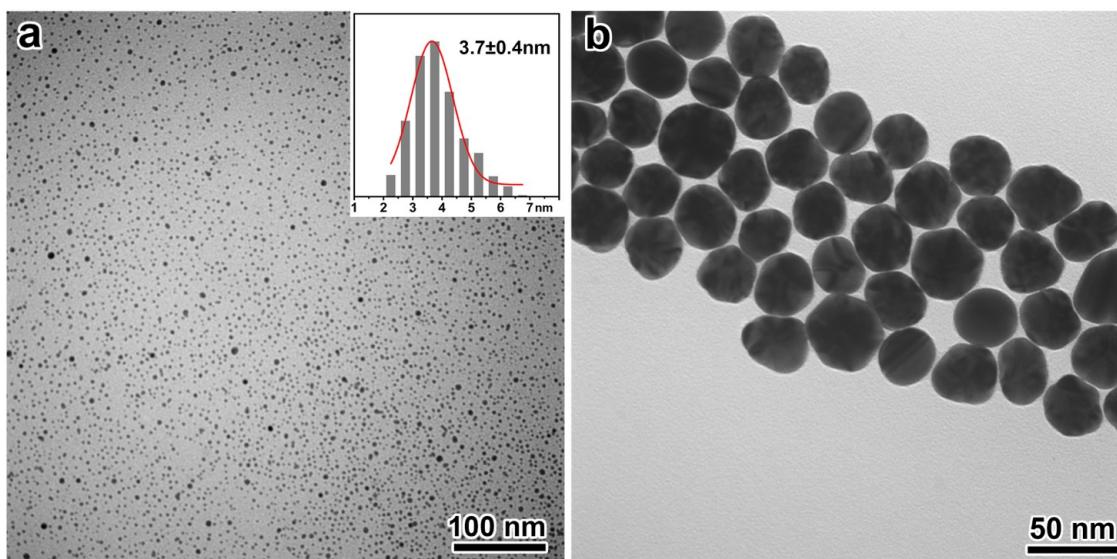
Figure S9. TEM images of Au nanospheres (a: ~ 3.7 nm, b: ~ 30 nm) for SERS analysis (Figure 4). Inset of (a): Size distributions of the Au nanoparticle measured from the TEM image.

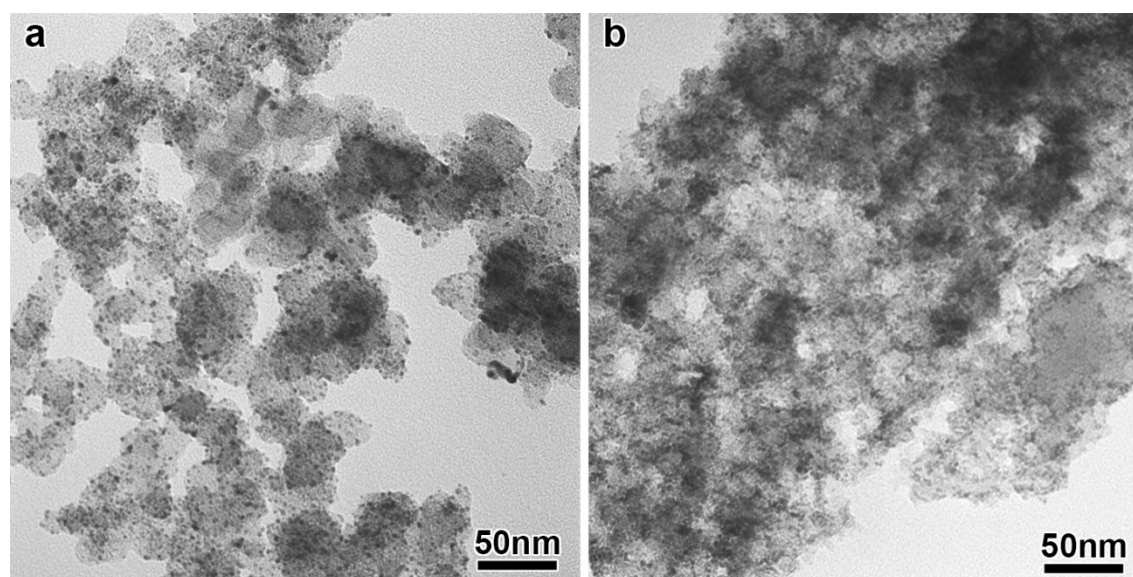**4. Supporting Information on the Electrochemical Experiments.**

Figure S10. (a–b) TEM image of the commercial Pt/C and Pd/C catalysts, respectively.
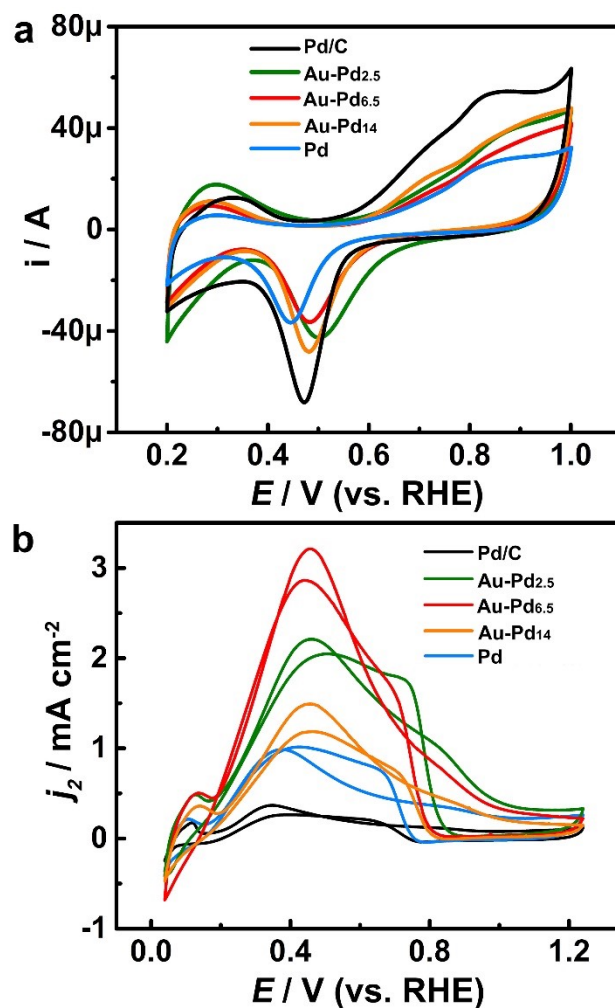
Figure S11. (a) ECSA calculation of the different catalyst by under-potential deposition (UPD) of Cu. CV curves of the catalysts in N_2-saturated H_2SO_4 (0.05 M) with $CuSO_4$ (0.05 M) at a scan rate of 5 mV·s^{-1} are presented. The ECSA of the catalysts were 80 (Pd/C), 46 (Au-Pd$_{2.5}$), 41 (Au-Pd$_{6.5}$), 53 (Au-Pd$_{14}$), and 43 m^2·g^{-1} (Pd), respectively. (b) CV measurements of the different catalysts in N_2-saturated HCOOH (0.25M)/H_2SO_4 (0.5M) (scan rate: 50 mV·s^{-1}) in comparison with Pd/C. Catalytic activities were evaluated per unit ECSA (specific activity).
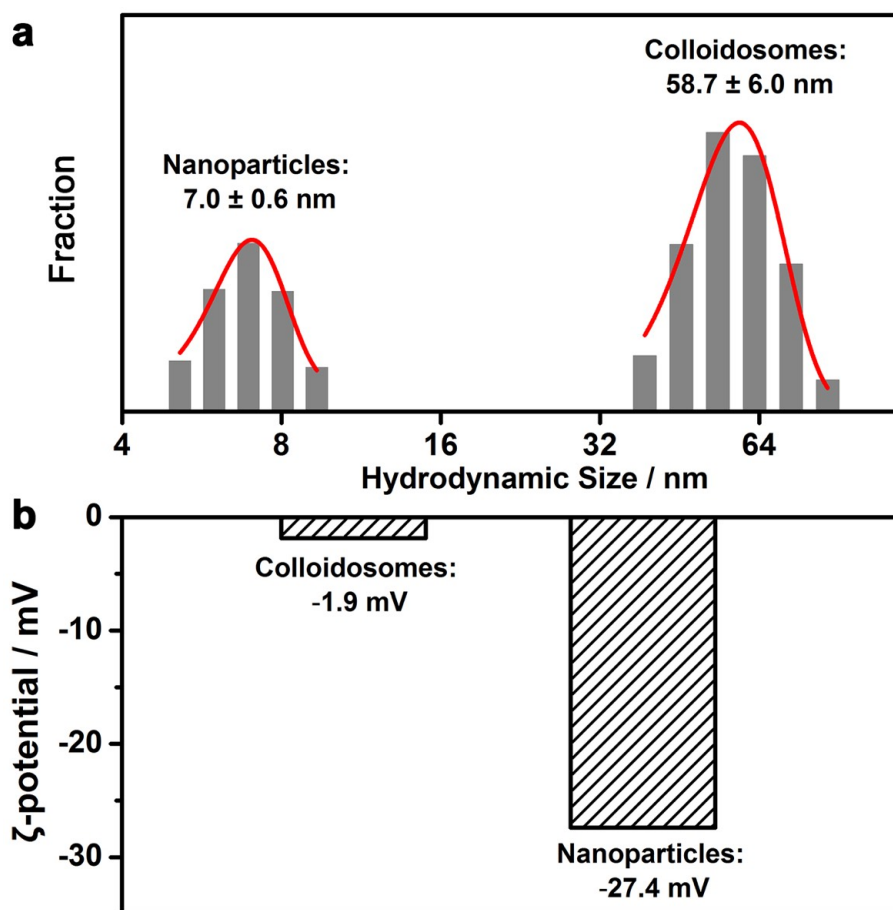
Figure S12. Hydrodynamic size distributions (a) and ζ-potentials (b) of the Au-Pd alloy colloidosomes before and after the disassembly. The hydrodynamic sizes are expressed by "mean ± standard deviation".
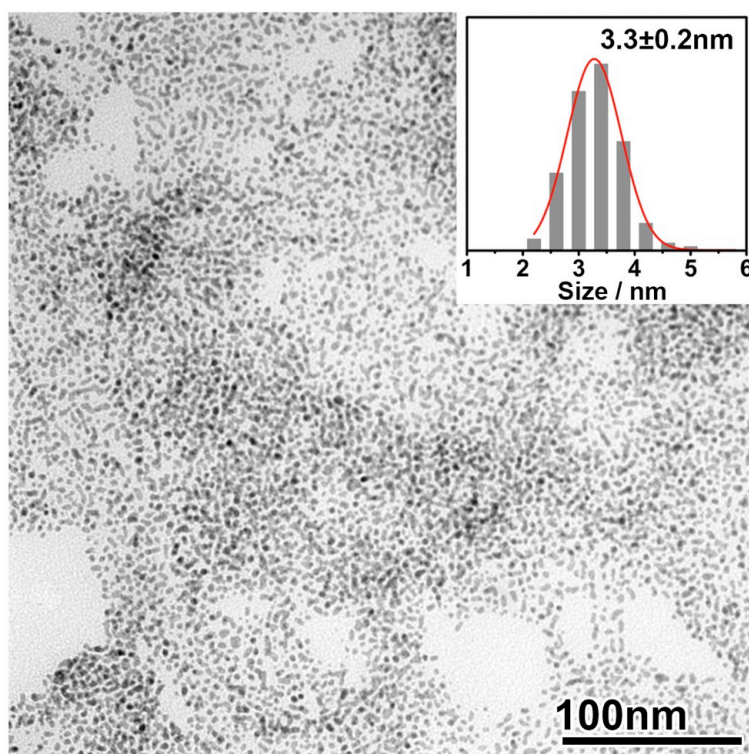
Figure S13. TEM image of the Au-Pd alloy nanoparticles obtained by disassembly of the colloidosomes. Inset: Size distributions of the Au-Pd alloy nanoparticles, measured from the TEM image.

Discussion on the disassembly of the Au-Pd alloy colloidosomes into nanoparticles (Figure S12-S13):

To reveal the effect of the nanoparticle assembly on the electrocatalytic activity of the colloidosomes, the Au-Pd alloy colloidosomes were disassembled into individual nanoparticles, with their electrocatalytic activities evaluated in FAOR. In a typical disassembly process, DEA was introduced into the colloidosomes. A ligand exchange process (PVP→DEA) occurred subsequently, with DEA adsorbing on the nanoparticle surface as a new ligand.[2] As a result, the nanoparticles became highly negatively charged, and the ζ-potential of the nanoparticles changed from near-neutral (PVP capping) to -27.4 mV (DEA capping, Figure S12b). The negative charges gave rise to strong repulsion forces between the primary nanoparticles, which overcame the energy reduction by the direct contact of the interparticle lattices, leading to disassembly of the colloidosomes into individual nanoparticles. The disassembly of the colloidosomes into primary nanoparticles can be evidenced by the DLS (Figure S12a), showing a shift of the hydrodynamic size from ~58.7 to ~7.0 nm, and more intuitionally by TEM (Figure S13), showing average size of ~3.3 nm of the nanoparticles after the disassembly. These results clearly confirmed the effectiveness of the DEA on disassembling the colloidosomes into individual nanoparticles.
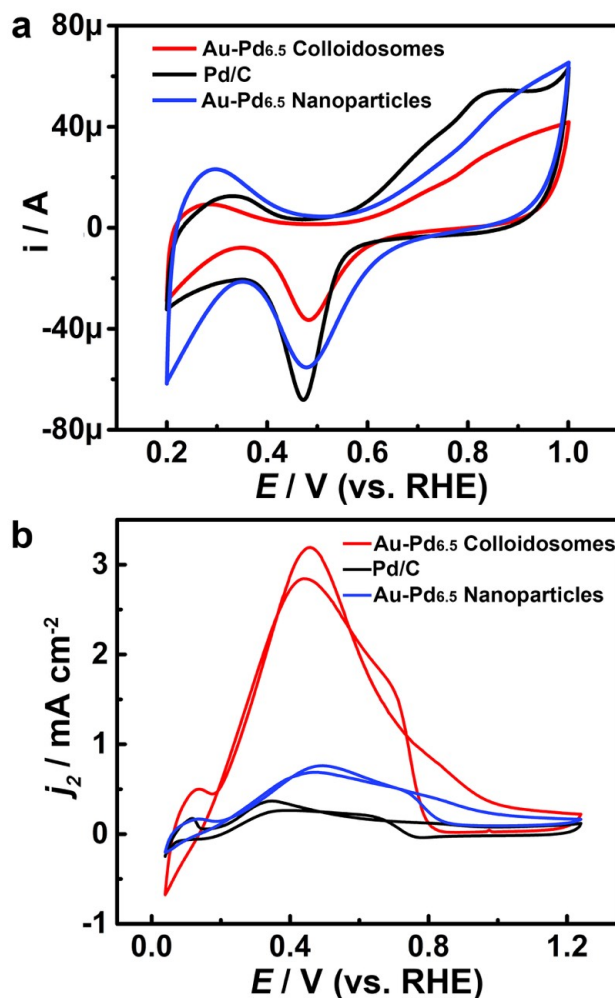
Figure S14. (a) ECSA calculation of the different catalyst by under-potential deposition (UPD) of Cu. CV curves of the catalysts in N_2-saturated H_2SO_4 (0.05 M) with $CuSO_4$ (0.05 M) at a scan rate of 5 mV·s^{-1} are presented. The ECSA of the catalysts were 0.80 (Pd/C), 0.41 (Au-Pd$_{6.5}$ colloidosomes), 0.67 (Au-Pd$_{6.5}$ nanoparticles), respectively. (b) CV measurements of the different catalysts in N_2-saturated HCOOH (0.25M)/H_2SO_4 (0.5M) (scan rate: 50 mV·s^{-1}) in comparison with Pd/C. Catalytic activities were evaluated per unit ECSA (specific activity).
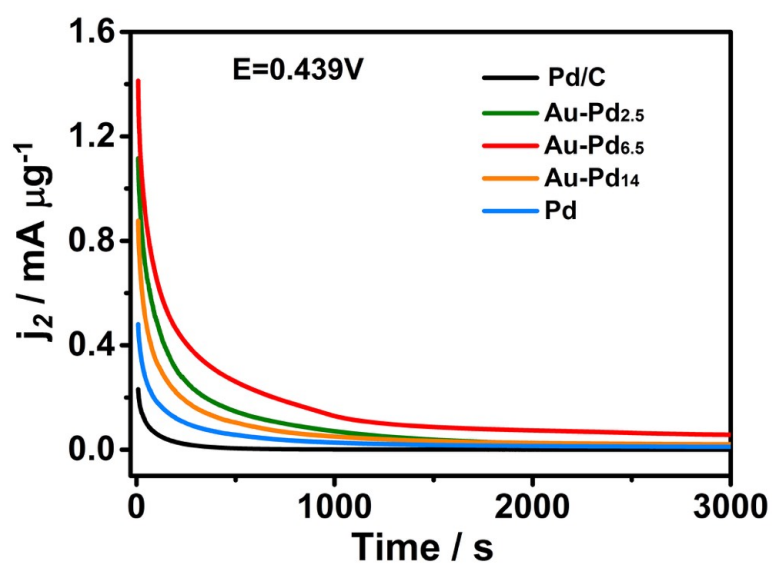
Figure S15. Chronoamperometry curves of the Pd and Au-Pd colloidosomes in N_2-saturated HCOOH(0.25 M)/H_2SO_4(0.5 M) at 0.439 V (vs. RHE). The chronoamperometry curve of Pd/C was listed for comparison. Compared with Pd colloidosomes, the Au-Pd alloy colloidosomes showed much increased catalytic stability due to the effective hindrance of CO poisoning by Au.

5. Extension: Synthesis and electrochemical catalytic property of Pd-Pt alloy colloidosomes

The versatility of the assembly strategy reported in this work can be exemplified by constructing Pd-Pt alloy colloidosomes. The Pd-Pt alloy colloidosomes were synthesized by self-assembly of PVP-capped Pd seeds at the interface of a PVP emulsion and subsequent growth of Pt on the Pd seeds (Figure S16). The Pd-Pt alloy nanoparticle grains were ~ 1.7 nm in size, determined from the TEM image and XRD pattern (Figure S16), with the Pt/Pd ratio being 2.17 determined by inductively coupled plasma mass spectrometry (ICP-MS) (Table S1). The Pd-Pt alloy colloidosomes were supported on carbon black (Cabot, Vulcan XC-72) with a Pt loading of ~20 % for ORR catalysis. Commercial Pt/C (JM, 20%Pt/XC72R, HiSPEC 3000, < 3.5 nm) was used as a benchmark (Figure S10). The ECSAs of the Pd-Pt alloy colloidosomes and Pt/C were 0.89 and 1.05 $cm^2 \cdot \mu g^{-1}$, respectively (Figure S18a–b). Figure S17b shows the positive-going ORR polarization curves of the catalysts. The specific and mass activities were calculated using the Koutecky-Levich equation, normalized against the ECSA and Pt mass of the catalysts (Figure S17c–d). Both the specific and mass activity of the Pd-Pt alloy colloidosomes were greatly enhanced compared with the commercial Pt/C. At 0.9 V vs RHE, the mass activity of the Pd-Pt alloy colloidosomes was 0.26 $mA \cdot \mu g^{-1}$, ~ 1.5 times that of the Pt/C (0.17 $mA \cdot \mu g^{-1}$). The specific activity of the Pt-Pd colloidosomes (0.30 $mA \cdot cm^{-2}$) at 0.9 V showed 1.88-fold enhancement compared with that of the Pt/C (0.16 $mA \cdot cm^{-2}$). The enhancement can be attributed to the synergistic effect arising from the contraction of the Pt lattice by alloying with Pd[3] and the abundant grain boundaries induced by the nanoparticle assembly in the Pd-Pt alloy colloidosomes. The difference in the size of the nanoparticle grains may also contribute to the markedly enhanced catalytic activity.

The Pd-Pt alloy colloidosomes also exhibited remarkable catalytic durability due to the self-supported nanostructure (Figure S18c–d). After 2000 cycles of linear potential sweeps (0.6–1.05 V, 0.05 V/s) in O_2-saturated 0.1 M $HClO_4$, the ECSA of the Pt-Pd alloy colloidosomes dropped by 9.7 %, while the ESCA drop of the Pt/C catalyst was ~ 48 %. Furthermore, the ORR mass activity of the Pt/C catalyst showed a remarkable degradation by ~ 50 % after 2000 cycles. In clear contrast, the ORR activity of the Pd-Pt alloy colloidosomes showed much less degradation (17 %) under the same conditions. These results demonstrate excellent activity and durability of the self-supported Pd-Pt alloy colloidosomes in ORR reactions.
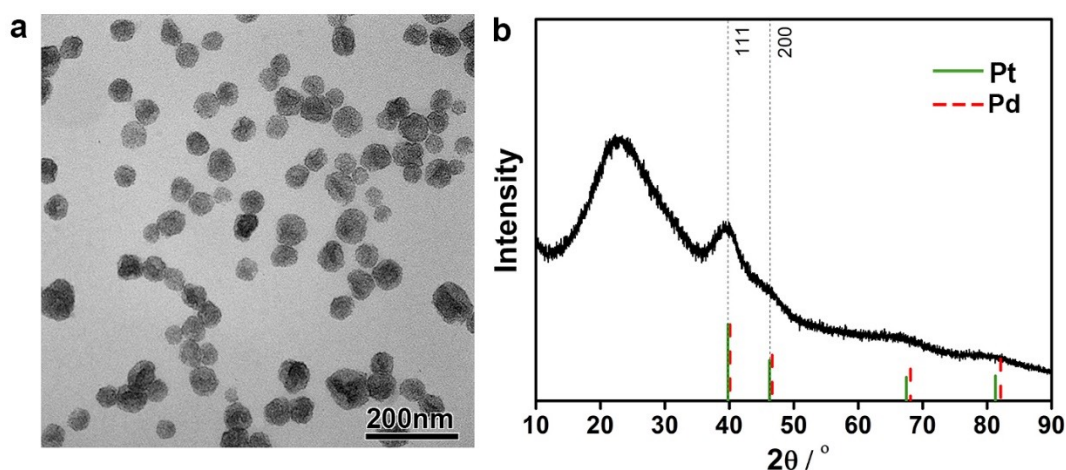

Figure S16. Characterization of the Pd-Pt alloy colloidosomes. (a) TEM image of the Pd-Pt alloy colloidosomes. (b) XRD pattern of the Pd-Pt alloy colloidosomes. Standard peak positions of Pt (JCPDF #04-0802) and Pd (JCPDF #46-1043) are shown for reference. The broad peaks at ~22° (2θ) was from the glass substrate.
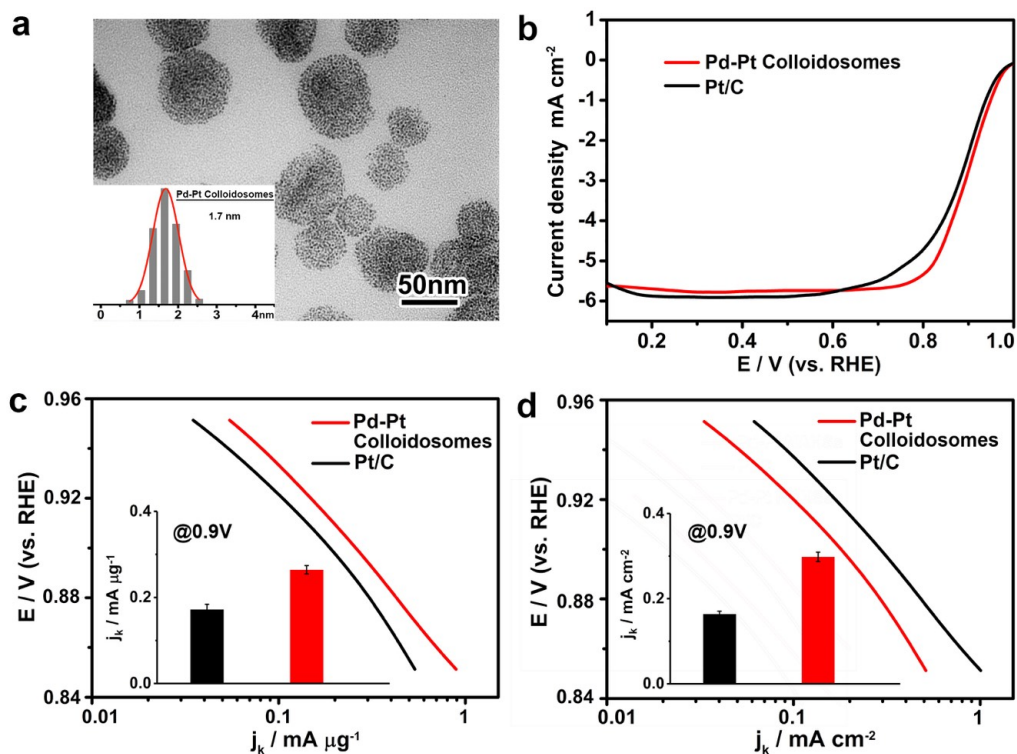
Figure S17. Synthesis of Pd-Pt alloy colloidosomes for ORR reactions. (a) TEM image of the Pd-Pt alloy colloidosomes. Inset: Size distributions of the primary Pd-Pt alloy nanoparticles. (b) ORR polarization curves of the Pd-Pt alloy colloidosomes and commercial Pt/C recorded from O_2-saturated $HClO_4$ (0.1 M) at a sweep rate of 10 mV·s^{-1} and a rotation rate of 1600 rpm. The current densities were normalized to the geometric area of the rotating disk electrode (0.196 cm^2). (c–d) Plots of the specific and mass activities given as kinetic current density (j_k) normalized to the ECSA and Pt mass, respectively. Error bars represent the standard deviation of the activities obtained from 3 independent measurements.
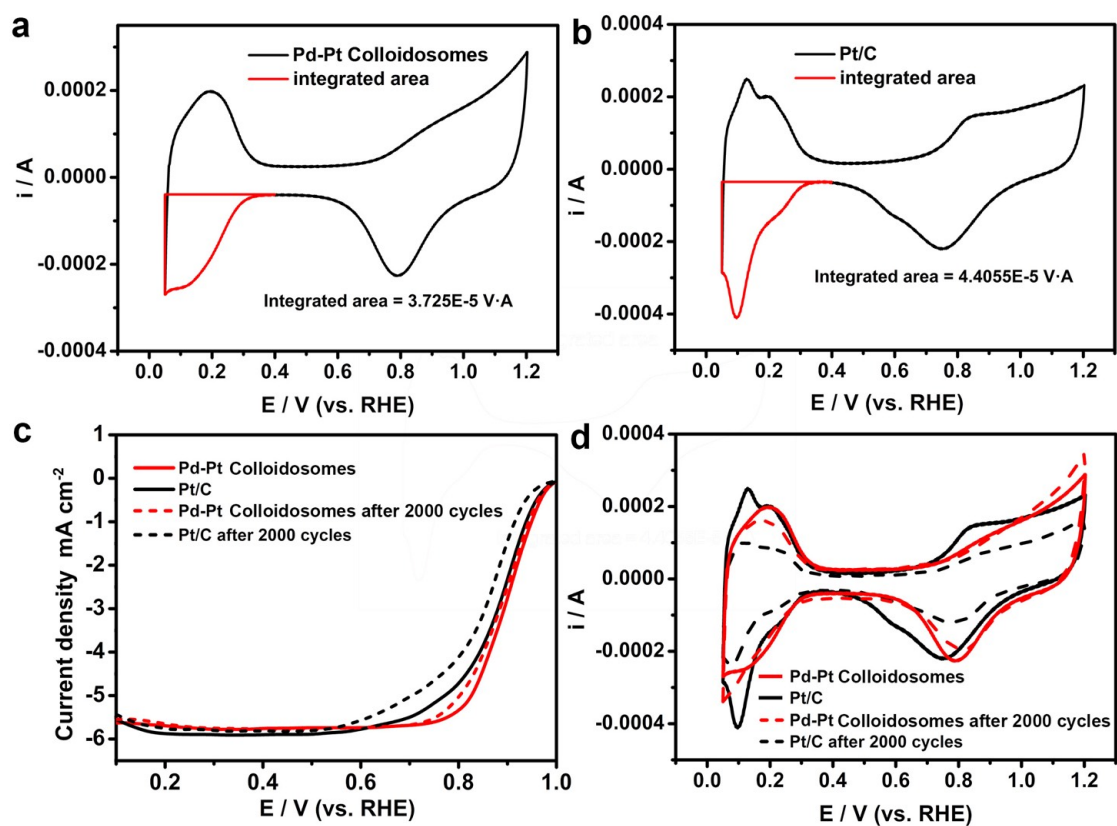
Figure S18. Additional results of the electrocatalysis with Pd-Pt alloy colloidosomes as the catalyst. (a–b) CV curves recorded in N_2-saturated 0.1 M $HClO_4$, with the Pd-Pt colloidosomes and commercial Pt/C being the catalyst, respectively. Scan rate: 50 mV·s^{-1}. The ECSAs were therefore estimated to be 0.89 (Pd-Pt colloidosomes) and 1.05 cm^2·µg^{-1} (Pt/C), respectively, from the charges associated with the desorption of hydrogen after double-layer correction with a reference value of 210 µC·cm^{-2}. (c) ORR polarization curves of the Pd-Pt colloidosomes and the Pt/C catalyst before and after 2000 cycles of the potential sweep (0.6–1.05 V) in O_2-saturated 0.1 M $HClO_4$ (Scan rate: 50 mV·s^{-1}; rotation speed: 1600 rpm). (d) CV curves of the Pd-Pt colloidosomes and the Pt/C catalyst in N_2-saturated 0.1 M $HClO_4$ before and after 2000 cycles of the potential sweep.

6. Extension: Synthesis and electrochemical catalytic property of Au-Pt alloy colloidosomes

The versatility of the assembly strategy reported in this work can be exemplified by constructing Au-Pt alloy colloidosomes. We prepared Au-Pt alloy colloidosomes by assembly of Au seeds at the interface of a PVP emulsion and consequent growth of Pt on these seeds. The Au-Pt colloidosomes are polycrystalline with abundant crystallites of small sizes (Figure S19a–c). XRD confirms that the Au-Pt colloidosomes are composed of an Au-Pt alloy (Figure S19e). The Au-Pt alloy colloidosomes showed particularly high catalytic activity in formic acid oxidation reactions (FAORs) (Figure S20). Compared with commercial Pt/C, the Au-Pt alloy colloidosomes favor the pathway of dehydrogenation rather than dehydration of formic acid, which shows much less prominent poisoning effect, and thus significantly enhanced specific activity and mass activity (Figure S20e). The improved electrocatalytic activity can be ascribed to the crystallographic defects in the Au-Pt colloidosomes, as well as the ligand effect with Au → Pt electron transfer which favors consequent electron back-donation to surface-adsorbed formic acid and thus greatly enhanced interaction. It also makes the formic acid molecules to adopt a bridging configuration on the metal surface, allowing for dehydrogenation pathways of the reaction. On the other hand, the Au-Pt colloidosomes are self-supported, rigid nanostructures, which enables high stability and durability in electrochemical catalytic FAOR reactions. The hollow interior and the porous shell of the colloidosomes facilitate the diffusion of the reagents around the small crystallites, which favors efficient utilization of Pt and thus high mass activity in FAOR reactions.
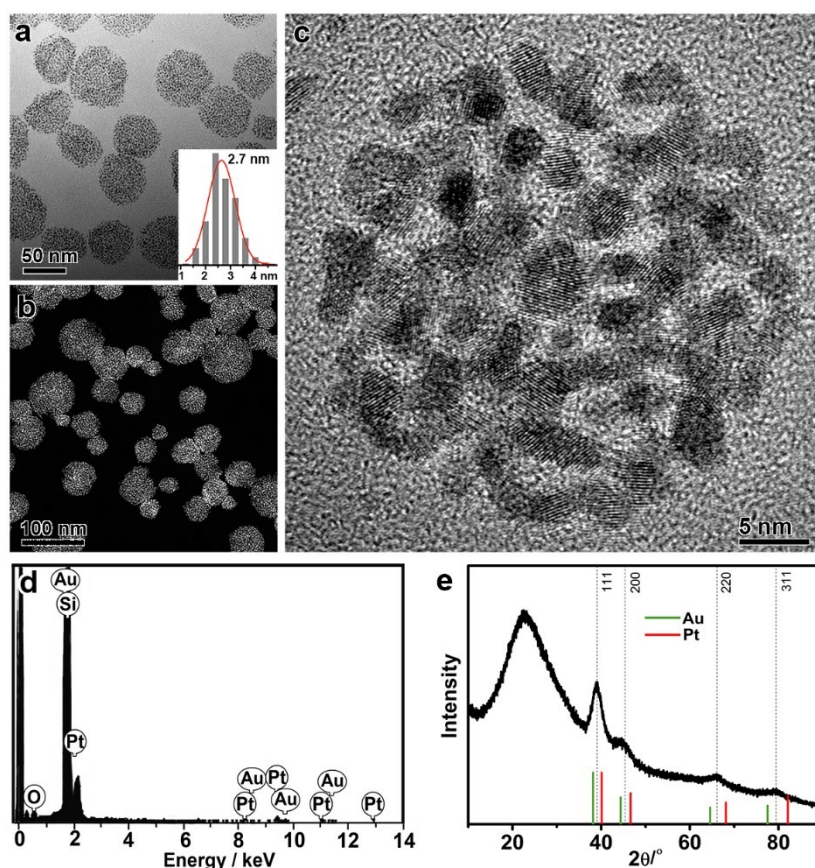
Figure S19. (a) TEM image of the Au-Pt colloidosomes. Inset: Size distribution of the primary Au-Pt alloy nanoparticles. (b) HAADF-STEM image of the Au-Pt colloidosomes, with bight dots showing nanoparticle grains. (c) HRTEM image of an individual Pt-Au colloidosome, confirming the polycrystallinity. (d) EDS of the Au-Pt colloidosomes after PVP removal. Signals from both Au and Pt can be detected. The signal of Si was from the silicon substrate. (e) XRD pattern of the Au-Pt colloidosomes. Standard peak positions of Au (JCPDF #04-0784) and Pt (JCPDF #04-0802) are shown for reference. The broad peaks around ~22° (2θ) are from glass substrate. The XRD pattern hints that the Au-Pt colloidosomes are composed of an Au-Pt alloy.
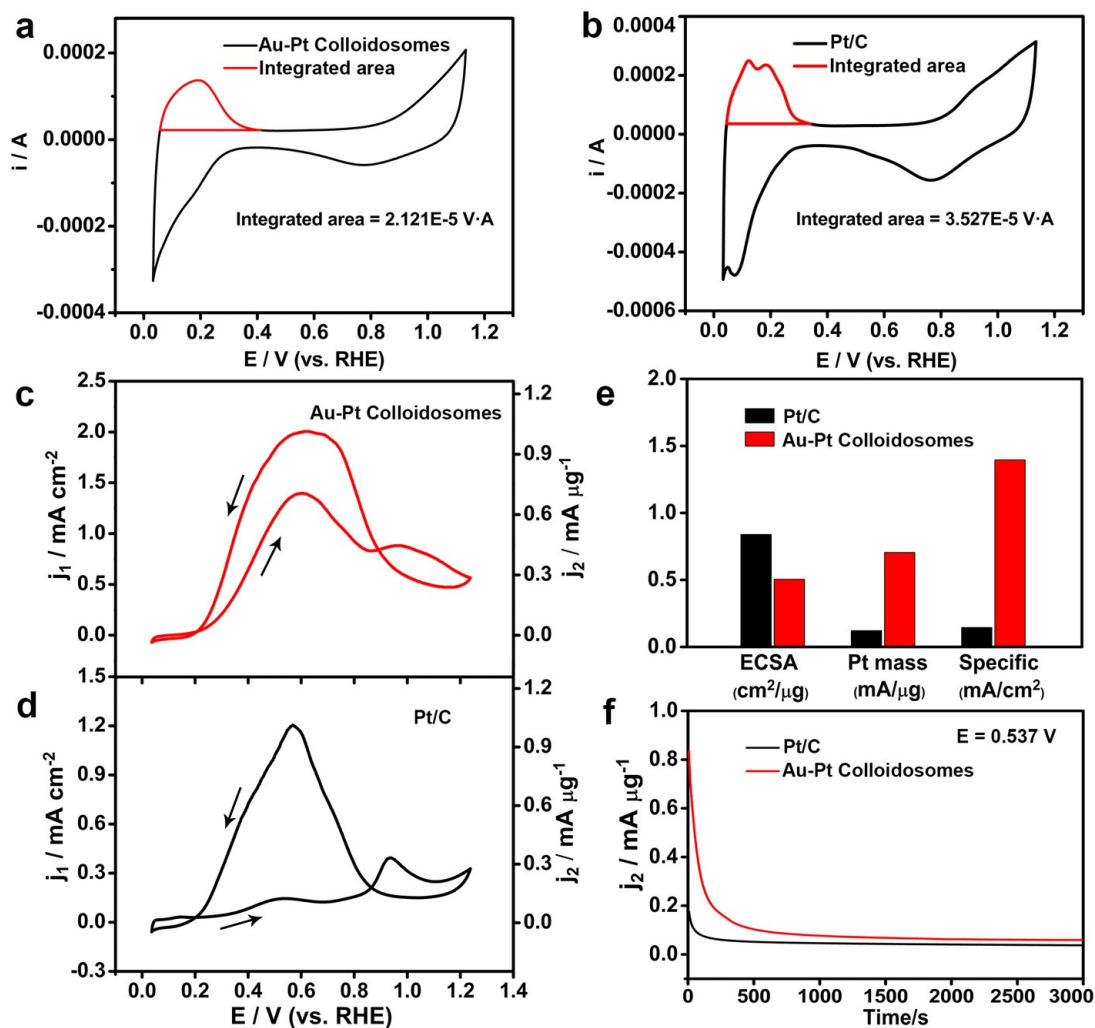
Figure S20. (a–b) CV curves of the Au-Pt colloidosomes and commercial Pt/C recorded in N_2-saturated 0.5 M H_2SO_4. Scan rate: 50 mV·s^{-1}. The ECSAs were therefore estimated to be 0.51 and 0.84 cm^2·µg^{-1}, respectively, from the charges associated with the desorption of hydrogen after double-layer correction with a reference value of 210 µC·cm^{-2}. (c–d) CVs of Au-Pt colloidosomes and commercial Pt/C catalysts, respectively, in 0.5 M H_2SO_4 with 0.25 M HCOOH. Scan rate: 50 mV·s^{-1}. Currents were normalized with respect to the ECSA (left axis) and the mass of Pt (right axis), respectively. (e) Comparison of the ECSA, Pt mass activity and specific activity of the catalysts. (f) Chronoamperometry curves of the Au-Pt colloidosomes and the Pt/C catalyst in N_2-saturated 0.5 M H_2SO_4 with 0.25 M HCOOH, at 0.537 V.
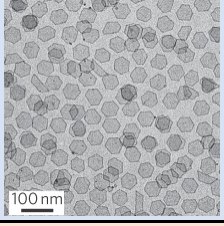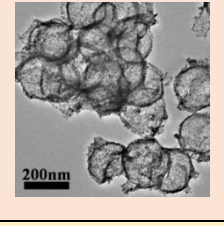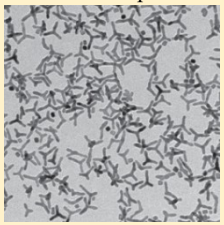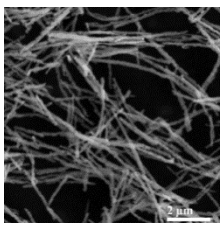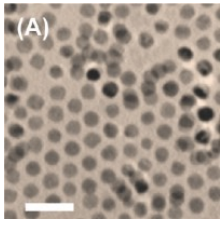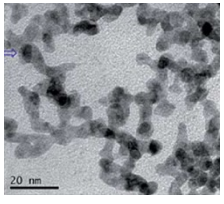
7. Comparison of the catalytic activity of the Au-Pd alloy colloidosomes in FAOR with the results from the literature.

Table S2. Typical specific and mass activities of Pd-based nanostructures for the electrocatalytic FAOR. Note: Data with asterisks (*) indicate that they are estimated from the figures in the reports; data in parentheses are obtained by calculation based on reported values of the mass/specific activity and the ECSA.
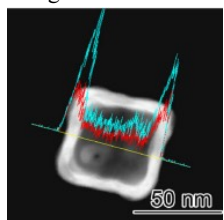
Entry	Mass Activity /mA μg^{-1}	Specific Activity /mA cm^{-2}	ECSA /m^2 g^{-1}	Reaction Medium	Reference and Nots
Au-Pd alloy colloidosomes	1.31	3.19	41	0.25 M HCOOH + 0.5 M H_2SO_4	ECSA was determined by underpotential deposition of Cu. **(Reported in this work)**
	1.31	1.90	69	0.25 M HCOOH + 0.5 M H_2SO_4	Reaction conditions were the same as those in reference [3]. ECSA was determined by adsorption of hydrogen in H_2SO_4.
	1.55	7.24	21	0.5 M HCOOH + 0.5 M H_2SO_4	Reaction conditions were the same as those in reference [4]. ECSA was determined by the reduction of Pd oxide in H_2SO_4.
	1.55	4.61	33.6	0.5 M HCOOH + 0.5 M H_2SO_4	Reaction conditions were the same as those in reference [13]. ECSA was determined by CO stripping.
	2.91	6.27	46.4	0.5 M HCOOH + 0.5 M $HClO_4$	Reaction conditions were the same as those in reference [5]. ECSA was determined by adsorption of hydrogen in $HClO_4$..
	3.53	19.6	18	0.5 M HCOOH + 0.1 M $HClO_4$	Reaction conditions were the same as those in reference [12]. ECSA was determined by desorption of the monolayer of oxygen in $HClO_4$.
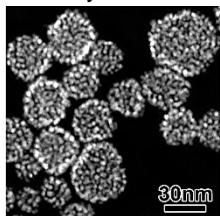
Material		Value 1	Value 2	Value 3	Electrolyte	Ref
Pd Nanosheets		1.38	(2.06)	67	0.25 M HCOOH + 0.5 M H_2SO_4	[4]
Graphene Hollow Nanosphere@Pd-Networks		0.97	(2.46)	39.3	0.5 M HCOOH + 0.5 M H_2SO_4	[5]
Pd-Cu Tripods		1.58	5.51	(28.7)	0.5 M HCOOH + 0.5 M $HClO_4$	[6]
Porous Pd-Ni Nanowire		~0.82*	/	/	0.5 M HCOOH + 0.5 M H_2SO_4	[7]
CoPd Nanoparticles		0.774	/	/	2 M HCOOH + 0.1 M $HClO_4$	[8]
PdNi Networks supported on graphene oxide		0.6	(0.61)	98.2	0.5 M HCOOH + 0.5 M H_2SO_4	[9]

Pd-Ag hollow structures 	~0.53*	/	/	0.1 M HCOOH + 0.1 M HClO$_4$	10
Pd arrow tripods 	0.4	2	20	0.5 M HCOOH + 0.5 M H$_2$SO$_4$	11
Au/Pd core-shell Nanoparticles 	0.48	/	/	0.1 M HCOOH + 0.1 M HClO$_4$	12
Au-Pd alloy Nanocrystals 	0.42	12.3	(3.4)	0.5 M HCOOH + 0.1 M HClO$_4$	13
Bi-Pd Nanotubes 	(0.45)	~4.5*	10	0.5 M HCOOH + 0.5 M H$_2$SO$_4$	14
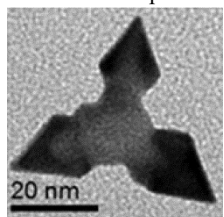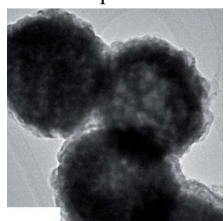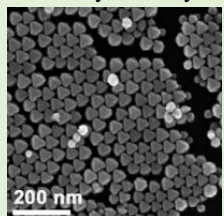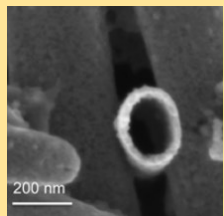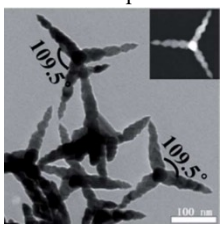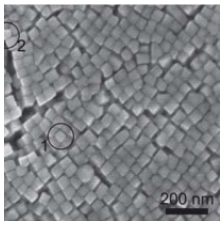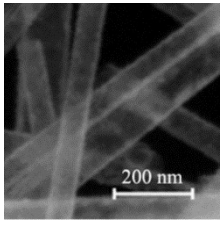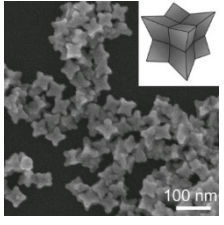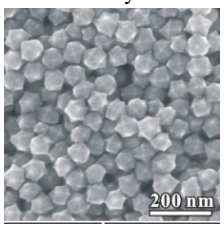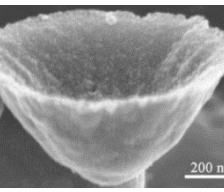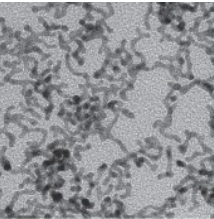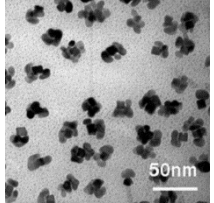
Pd tetrapods	0.365	2.3	(15.9)	0.5 M HCOOH + 0.5 M H_2SO_4	15
Pd cubes	~0.26*	/	/	0.5 M HCOOH + 0.1 M $HClO_4$	16
Hollow Ag@Pd core–shell nanotubes	~0.25*	/	/	0.5 M HCOOH + 0.5 M H_2SO_4	17
Au–Pd Alloy Octapods	/	~3.4*	/	0.25 M HCOOH + 0.5 M H_2SO_4	18
Hexoctahedral Au-Pd Alloy Nanocrystal	/	~3.3*	/	0.25 M HCOOH + 0.5 M H_2SO_4	19
Pd-Au hollow cone-like microstructure	/	2.9	/	1 M HCOOH + 1 M HCOOK	20

Pd Nanowires/C	/	2.4	/	2 M HCOOH + 0.1 M HClO$_4$	21
Binary Pt/Pd Nanoparticles	/	~1.9*	/	0.25 M HCOOH + 0.5 M H$_2$SO$_4$	22

Discussion:

Representative reports published in recent years on Pd-based nanocrystals for the electrocatalytic FAOR have been listed in Table S2. Because the reaction media (*e.g.* concentration of formic acid, type and concentration of the acid electrolyte) and the methods (*e.g.*, way to determine the ECSA) vary a lot from one report to another, it is difficult to compare our results with the reported values. We therefore conducted the electrocatalysis according to typical literature-reported procedures with the same reaction medium and method. It can be inferred that our results are comparable to, if not higher than the highest values reported in literature. Our materials represent superior electrocatalysts for the electrochemical FAOR with excellent specific and mass activities.

One of the best Pt-based nanocatalysts for the electrocatalytic FAOR was monocrystalline PtBi intermetallics, according to a recent report.[23] In this report, OMC-PtBi-3 nm exhibited a very high mass activity of 770 mA·mg^{-1} at 0.57 V. This value cannot be directly compared with the values reported in this work due to the different conditions in the measurement. Therefore, we adopted the same reaction conditions for the FAOR reaction with our Au-Pd alloy colloidosomes as the catalyst. The mass activity of the Au-Pd alloy colloidosomes in FAOR turned out to be 906 mA·mg^{-1}, which is much larger than that recorded in this report. Moreover, the maximal mass-activity has been achieved at 0.45 V vs RHE, which is much lower than that in this report (> 0.57 V), meaning that the FAOR proceeds more easily by using Au-Pd colloidosomes as the catalyst.

Based on these comparisons, it can be inferred that the Au-Pd alloy colloidosomes is among the best catalysts reported so far for the electrocatalytic FAOR.

References

1. (a) Lim, B.; Jiang, M.; Camargo, P. H. C.; Cho, E. C.; Tao, J.; Lu, X.; Zhu, Y.; Xia, Y., Pd-Pt Bimetallic Nanodendrites with High Activity for Oxygen Reduction. *Science* **2009,** *324* (5932), 1302-1305; (b) Shao, M.; Odell, J. H.; Choi, S.-I.; Xia, Y., Electrochemical surface area measurements of platinum- and palladium-based nanoparticles. *Electrochem. Commun.* **2013,** *31*, 46-48.

2. Fan, Q.; Liu, K.; Liu, Z.; Liu, H.; Zhang, L.; Zhong, P.; Gao, C., A Ligand-Exchange Route to Noble Metal Nanocrystals with a Clean Surface for Enhanced Optical and Catalytic Properties. *Part. Part. Syst. Charact.* **2017**, DOI: 10.1002/ppsc.201700075.

3. Wang, X.; Figueroa-Cosme, L.; Yang, X.; Luo, M.; Liu, J.; Xie, Z.; Xia, Y., Pt-Based Icosahedral Nanocages: Using a Combination of {111} Facets, Twin Defects, and Ultrathin Walls to Greatly Enhance Their Activity toward Oxygen Reduction. *Nano Lett.* **2016,** *16* (2), 1467-71.

4. Huang, X.; Tang, S.; Mu, X.; Dai, Y.; Chen, G.; Zhou, Z.; Ruan, F.; Yang, Z.; Zheng, N., Freestanding palladium nanosheets with plasmonic and catalytic properties. *Nat. Nanotechnol.* **2011,** *6* (1), 28-32.

5. Qiu, X.; Wu, P.; Xu, L.; Tang, Y.; Lee, J.-M., 3D Graphene Hollow Nanospheres@Palladium-Networks as an Efficient Electrocatalyst for Formic Acid Oxidation. *Adv. Mater. Interfaces* **2015,** *2* (18), 1500321.

6. Zhang, L.; Choi, S.-I.; Tao, J.; Peng, H.-C.; Xie, S.; Zhu, Y.; Xie, Z.; Xia, Y., Pd-Cu Bimetallic Tripods: A Mechanistic Understanding of the Synthesis and Their Enhanced Electrocatalytic Activity for Formic Acid Oxidation. *Adv. Funct. Mater.* **2014,** *24* (47), 7520-7529.

7. Du, C.; Chen, M.; Wang, W.; Yin, G., Nanoporous PdNi Alloy Nanowires As Highly Active Catalysts for the Electro-Oxidation of Formic Acid. *ACS Appl. Mater. Interfaces* **2011,** *3* (2), 105-9.

8. Mazumder, V.; Chi, M.; Mankin, M. N.; Liu, Y.; Metin, O.; Sun, D.; More, K. L.; Sun, S., A facile synthesis of MPd (M = Co, Cu) nanoparticles and their catalysis for formic acid oxidation. *Nano Lett.* **2012,** *12* (2), 1102-6.

9. Bin, D.; Yang, B.; Ren, F.; Zhang, K.; Yang, P.; Du, Y., Facile synthesis of PdNi nanowire networks supported on reduced graphene oxide with enhanced catalytic performance for formic acid oxidation. *J. Mater. Chem. A* **2015,** *3* (26), 14001-14006.

10. Liu, D.; Xie, M.; Wang, C.; Liao, L.; Qiu, L.; Ma, J.; Huang, H.; Long, R.; Jiang, J.; Xiong, Y., Pd-Ag alloy hollow nanostructures with interatomic charge polarization for enhanced electrocatalytic formic acid oxidation. *Nano Res.* **2016,** *9* (6), 1590-1599.

11. Su, N.; Chen, X.; Ren, Y.; Yue, B.; Wang, H.; Cai, W.; He, H., The facile synthesis of single crystalline palladium arrow-headed tripods and their application in formic acid electro-oxidation. *Chem. Commun.* **2015,** *51* (33), 7195-8.

12. Hsu, C.; Wei, M.; Wei, Z.; Liu, F., Improving the catalytic activity of Au/Pd core–shell nanoparticles with a tailored Pd structure for formic acid oxidation reaction. *RSC Adv.* **2016,** *6* (29), 24645-24650.

13. Hong, J. W.; Kim, D.; Lee, Y. W.; Kim, M.; Kang, S. W.; Han, S. W., Atomic-distribution-dependent electrocatalytic activity of Au-Pd bimetallic nanocrystals. *Angew. Chem. Int. Ed.* **2011,** *50* (38), 8876-80.

14. Atkinson, R. W.; St. John, S.; Dyck, O.; Unocic, K. A.; Unocic, R. R.; Burke, C. S.; Cisco, J. W.; Rice, C. A.; Zawodzinski, T. A.; Papandrew, A. B., Supportless, Bismuth-Modified Palladium Nanotubes with Improved Activity and Stability for Formic Acid Oxidation. *ACS Catal.* **2015,** *5* (9), 5154-5163.

15. Zhao, R.; Fu, G.; Zhou, T.; Chen, Y.; Zhu, X.; Tang, Y.; Lu, T., Multi-generation overgrowth induced synthesis of three-dimensional highly branched palladium tetrapods and their electrocatalytic activity for formic acid oxidation. *Nanoscale* **2014,** *6* (5), 2776-81.

16. Zhang, X.; Yin, H.; Wang, J.; Chang, L.; Gao, Y.; Liu, W.; Tang, Z., Shape-dependent electrocatalytic activity of monodispersed palladium nanocrystals toward formic acid oxidation. *Nanoscale* **2013,** *5* (18), 8392-7.

17. Jiang, Y.; Lu, Y.; Han, D.; Zhang, Q.; Niu, L., Hollow Ag@Pd core-shell nanotubes as highly active catalysts for the electro-oxidation of formic acid. *Nanotechnology* **2012,** *23* (10), 105609.

18. Wang, L.-B.; Wang, Y.-C.; Guo, H.-Y.; Huang, J.-L.; Zhao, Y.-L.; Liu, Q.-Y.; Wu, X.; Zeng, J., Au-Pd Alloy Octapods with High Electrocatalytic Activity for the Oxidation of Formic Acid. *Part. Part. Syst. Char.* **2015,** *32* (3), 295-300.

19. Zhang, L.; Zhang, J.; Kuang, Q.; Xie, S.; Jiang, Z.; Xie, Z.; Zheng, L., Cu^{2+}-assisted synthesis of hexoctahedral Au-Pd alloy nanocrystals with high-index facets. *J. Am. Chem. Soc.* **2011,** *133* (43), 17114-7.

20. Li, L.; E, Y.; Yuan, J.; Luo, X.; Yang, Y.; Fan, L., Electrosynthesis of Pd/Au hollow cone-like microstructures for electrocatalytic formic acid oxidation. *Electrochim. Acta* **2011,** *56* (17), 6237-6244.

21. Wang, Y.; Choi, S.-I.; Zhao, X.; Xie, S.; Peng, H.-C.; Chi, M.; Huang, C. Z.; Xia, Y., Polyol Synthesis of Ultrathin Pd Nanowires via Attachment-Based Growth and Their Enhanced Activity towards Formic Acid Oxidation. *Adv. Funct. Mater.* **2014,** *24* (1), 131-139.

22. Lee, H.; Habas, S. E.; Somorjai, G. A.; Yang, P., Localized Pd Overgrowth on Cubic Pt Nanocrystals for Enhanced Electrocatalytic Oxidation of Formic Acid. *J. Am. Chem. Soc.* **2008,** *130* (16), 5406-5407.

23. Ji, X.; Lee, K. T.; Holden, R.; Zhang, L.; Zhang, J.; Botton, G. A.; Couillard, M.; Nazar, L. F., Nanocrystalline intermetallics on mesoporous carbon for direct formic acid fuel cell anodes. *Nat. Chem.* **2010,** *2* (4), 286-293.